LETTERS

Demonstration of two-qubit algorithms with a superconducting quantum processor

L. DiCarlo[1], J. M. Chow[1], J. M. Gambetta[2], Lev S. Bishop[1], B. R. Johnson[1], D. I. Schuster[1], J. Majer[3], A. Blais[4], L. Frunzio[1], S. M. Girvin[1] & R. J. Schoelkopf[1]

Quantum computers, which harness the superposition and entanglement of physical states, could outperform their classical counterparts in solving problems with technological impact—such as factoring large numbers and searching databases[1,2]. A quantum processor executes algorithms by applying a programmable sequence of gates to an initialized register of qubits, which coherently evolves into a final state containing the result of the computation. Building a quantum processor is challenging because of the need to meet simultaneously requirements that are in conflict: state preparation, long coherence times, universal gate operations and qubit readout. Processors based on a few qubits have been demonstrated using nuclear magnetic resonance[3–5], cold ion trap[6,7] and optical[8] systems, but a solid-state realization has remained an outstanding challenge. Here we demonstrate a two-qubit superconducting processor and the implementation of the Grover search and Deutsch–Jozsa quantum algorithms[1,2]. We use a two-qubit interaction, tunable in strength by two orders of magnitude on nanosecond timescales, which is mediated by a cavity bus in a circuit quantum electrodynamics architecture[9,10]. This interaction allows the generation of highly entangled states with concurrence up to 94 per cent. Although this processor constitutes an important step in quantum computing with integrated circuits, continuing efforts to increase qubit coherence times, gate performance and register size will be required to fulfil the promise of a scalable technology.

Over the past decade, superconducting circuits[11] have made considerable progress in all the requirements necessary for an electrically controlled, solid-state quantum computer. Coherence times[11,12] have risen by three orders of magnitude to ~1 μs, single-qubit gates[13,14] have reached error rates of 1%, engineered interactions[15–17] have produced two-qubit entanglement at a level of 60% concurrence[18], and qubit readout[18–20] has attained measurement fidelities of ~90%. However, combining these achievements in a single device remains challenging. One approach to integration is the quantum bus architecture[9,21,22], which uses a transmission line cavity to couple, control and measure qubits. We augment the architecture described in ref. 22 with flux-bias lines that tune individual qubit frequencies, permitting single-qubit phase gates. By pulsing the qubit frequencies to an avoided crossing where a $\sigma_z \otimes \sigma_z$ interaction turns on (σ_z is the Pauli z-operator), we are able to realize a two-qubit conditional phase (C-Phase) gate. Operation in the strong-dispersive regime[23] of circuit quantum electrodynamics (cQED) allows joint readout[24] that efficiently detects two-qubit correlations. Combined with single-qubit rotations, this enables tomography of the two-qubit state. Through improved understanding of spontaneous emission[25] and careful microwave engineering, we now attain state-of-the-art ~1 μs coherence times in a two-qubit device. This allows sufficient time to concatenate ~10 gates, realizing simple algorithms with fidelity greater than 80%.

Our processor, shown in Fig. 1a, is a four-port superconducting device comprising two transmon qubits[12,26] (Q_L and Q_R) inside a microwave cavity bus, and flux-bias lines proximal to each qubit. The cavity, normally off-resonance with the qubit transition frequencies f_L and f_R, couples the qubits by virtual photon exchange and shields them from the electromagnetic continuum. As previously demonstrated[22], microwave pulses resonant with f_L or f_R applied to the cavity input port provide frequency-multiplexed single-qubit x- and y-rotations with high fidelity[14] and selectivity. Pulsed measurement of the homodyne voltage V_H on the cavity output port provides qubit readout. The remaining two ports create local magnetic fields that tune the qubit transition frequencies. Each qubit has a split Josephson junction, so its frequency f depends on the flux Φ through the loop according to $hf \approx \sqrt{8E_C E_J^{max}|\cos(\pi\Phi/\Phi_0)|} - E_C$, where E_C is the charging energy, E_J^{max} is the maximum Josephson energy, h is Planck's constant, and Φ_0 is the flux quantum. By using short-circuited transmission lines with a bandwidth from d.c. to 2 GHz, we can tune f_L and f_R by many GHz using room temperature voltages V_L and V_R. Static tuning of qubit transitions using the flux-bias lines is demonstrated in Fig. 1b.

The spectrum of single excitations (Fig. 1b) shows the essential features of the cavity-coupled two-qubit Hamiltonian and allows determination of the relevant system parameters (see Methods). When the qubits are tuned to their maximum frequencies, point I, they are far detuned from the cavity and from each other, so that interactions are small. This point is therefore used for state preparation, single-qubit rotations and measurement, in the computational basis $|0, 0\rangle$, $|0, 1\rangle$, $|1, 0\rangle$ and $|1, 1\rangle$, where $|l, r\rangle$ denotes excitation level l (r) for Q_L (Q_R). Operation at this point is also desirable because it is a flux 'sweet spot'[12] for both qubits, providing long coherence, with relaxation and dephasing times $T_{1,L(R)} = 1.3(0.8)$ μs and $T^*_{2,L(R)} = 1.8(1.2)$ μs, respectively. Tuning Q_R into resonance with the cavity, point IV in Fig. 1b, reveals a vacuum Rabi splitting[10] from which the qubit–cavity interaction strength is extracted. Tuning Q_R into resonance with Q_L, point III, shows an avoided crossing resulting from a cavity-mediated, qubit–qubit transverse interaction[9,27] investigated previously[22]. In this work, we perform two-qubit gates at point II, where no interactions are immediately apparent on examining the one-excitation manifold.

However, a useful two-qubit interaction is revealed in the two-excitation spectrum, Fig. 2a. As V_R is swept away from point I, the non-computational higher-level transmon excitation $|0, 2\rangle$ decreases more rapidly than the computational state $|1, 1\rangle$, and these states would become degenerate at point II. But as shown in Fig. 2b, there is a large (160 MHz) cavity-mediated interaction between these

[1]Departments of Physics and Applied Physics, Yale University, New Haven, Connecticut 06511, USA. [2]Department of Physics and Astronomy and Institute for Quantum Computing, University of Waterloo, Waterloo, Ontario N2L 3G1, Canada. [3]Atominstitut der Österreichischen Universitäten, TU-Wien, A-1020 Vienna, Austria. [4]Département de Physique, Université de Sherbrooke, Sherbrooke, Québec J1K 2R1, Canada.

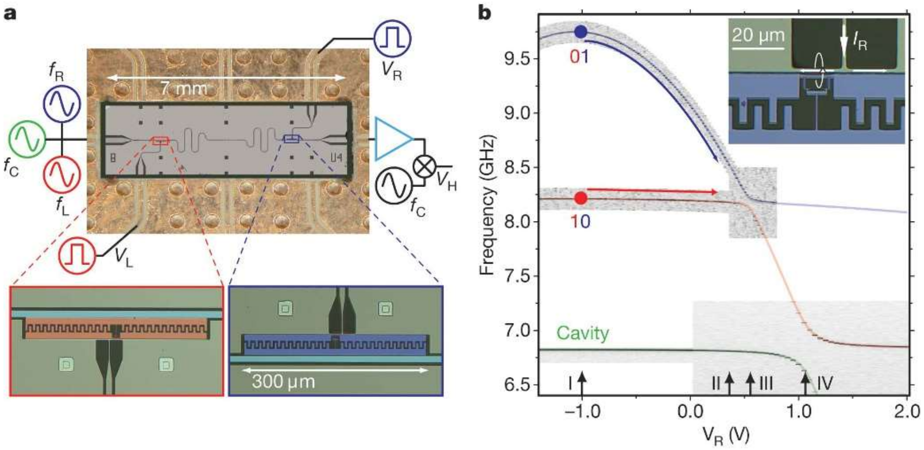

Figure 1 | Two-qubit cQED device, and cavity/qubit characterization. **a**, Optical micrograph of four-port device with a coplanar waveguide cavity bus coupling transmon qubits Q_L and Q_R (coloured red and blue in insets), and local flux-bias lines providing fast qubit tuning. Microwave pulses at the qubit transition frequencies f_L and f_R drive single-qubit rotations, and a pulsed measurement of the cavity homodyne voltage V_H (at frequency f_C) provides two-qubit readout. The flux-bias lines (bottom-left and top-right ports) are coplanar waveguides with short-circuit termination next to their target qubit. The termination geometry allows currents (I_L and I_R) on the lines to couple flux through the split junctions (**b**, inset). **b**, Grey-scale images of cavity transmission and of qubit spectroscopy as a function of V_R, showing local tuning of Q_R across the avoided crossing with Q_L (point III) and across the vacuum Rabi splitting with the cavity (point IV). Semi-transparent lines are theoretical best fits obtained from numerical diagonalization of a generalized Tavis–Cummings Hamiltonian[28]. Points I and II are the operating points of the processor. Preparation, single-qubit operations and measurements are performed at point I, and a C-Phase gate is achieved by pulsing into point II. Numerals indicate excitation level of Q_L (red) and Q_R (blue) in the spectroscopy at point I.

levels, producing a frequency shift $\zeta/2\pi$ of the lower branch with respect to the sum $f_L + f_R$, in good agreement with a numerical diagonalization of the generalized Tavis–Cummings Hamiltonian[28] (see Methods).

This shift is the mechanism of our conditional phase gate. Flux pulses, adiabatic with respect to the $|1,1\rangle \leftrightarrow |0,2\rangle$ avoided crossing, produce phase gates

$$U = \begin{pmatrix} 1 & 0 & 0 & 0 \\ 0 & e^{i\phi_{01}} & 0 & 0 \\ 0 & 0 & e^{i\phi_{10}} & 0 \\ 0 & 0 & 0 & e^{i\phi_{11}} \end{pmatrix}$$

in the computational Hilbert space. Here, $\phi_{lr} = 2\pi\int \delta f_{lr}(t)\mathrm{d}t$ is the dynamical phase acquired by $|l, r\rangle$, and δf_{lr} is the deviation of f_{lr} from its value at point I. A V_R pulse into point II such that $\int \zeta(t)\mathrm{d}t = (2n+1)\pi$ with integer n implements a C-Phase gate, because $\phi_{11} = \phi_{01} + \phi_{10} - \int\zeta(t)\mathrm{d}t$. This method of realizing a C-Phase gate by adiabatically using the avoided crossing between computational and non-computational states is generally applicable to qubit implementations with finite anharmonicity, such as transmons[12] or phase qubits[13]. A similar approach involving higher excitation levels but with non-adiabatic pulses was previously proposed[29]. The negative anharmonicity permits the phase gate at point II to occur before the onset of transverse coupling at point III.

Control of ζ by two orders of magnitude provides an excellent on-off ratio for the C-Phase gate. Measurements of ζ obtained from spectroscopy and from time-domain experiments show very good agreement (Fig. 2c). The time-domain method measures the difference in the precession frequency of Q_L in two Ramsey-style experiments, where a V_R-pulse of varying duration (0–100 ns) is inserted between $\pi/2$ rotations of Q_L, with Q_R either in the ground state $|0\rangle$ or excited into state $|1\rangle$. Using the time-domain approach, we measure a residual $\zeta/2\pi \approx 1.2$ MHz at point I (star in Fig. 2c). The theoretical ζ obtained by numerical diagonalization shows reasonable agreement with the data, except for a scale factor that is probably due to higher modes of the cavity[25], not included in the calculation.

The controlled phase interaction allows universal two-qubit gates. As an example, we produce entangled states on demand (Fig. 3). The pulse sequence in Fig. 3a generates any of the four Bell states,

$$|\Psi^{\pm}\rangle = \tfrac{1}{\sqrt{2}}(|0,0\rangle \pm |1,1\rangle) \quad |\Phi^{\pm}\rangle = \tfrac{1}{\sqrt{2}}(|0,1\rangle \pm |1,0\rangle)$$

depending on the choice of C-Phase gate cU_{ij} applied ($cU_{ij}|l,r\rangle = (-1)^{\delta_{il}\delta_{jr}}|l,r\rangle$, where δ is Kronecker's delta). We achieve $\int\zeta(t)\mathrm{d}t = \pi$ by tuning the amplitude of a 30 ns V_R-pulse close to point II and back. During the pulse, Q_R acquires a large dynamical phase $\phi_{01} \approx -60\pi$. The four cU_{ij} gates differ by whether ϕ_{01} and ϕ_{10} are even or odd multiples of π. We tune ϕ_{01} over a 2π range by adjusting the rising and falling edges of the pulse, and ϕ_{10} by varying the amplitude of a simultaneous weak V_L-pulse (Supplementary Fig. 3). The conditional phase $\int\zeta(t)\mathrm{d}t$ is largely independent of these two adjustments.

To detect the entanglement, we reconstruct the two-qubit density matrix ρ by quantum state tomography using joint dispersive readout[9,22,24]. A pulsed measurement of the homodyne voltage V_H measures the operator:

$$M = \beta_1\sigma_z^L + \beta_2\sigma_z^R + \beta_{12}\sigma_z^L \otimes \sigma_z^R$$

Operation in the strong-dispersive regime[23,24] makes the three constant coefficients have approximately the same magnitude, $|\beta_{12}| \approx |\beta_1|, |\beta_2|$, enhancing sensitivity to two-qubit correlations. A complete set of 15 linearly independent operators is built using single-qubit rotations before measuring M. An ensemble average of each operator is obtained by executing the sequence in Fig. 3a 450,000 times. The 15 average values are then input to a maximum-likelihood estimator of ρ (Supplementary Information).

The inferred density matrices ρ_{ml} reveal in all four cases (Fig. 3b–e) a high degree of two-qubit entanglement, which we quantify using concurrence[30], C. Values are listed in Fig. 3 legend, along with the metrics of purity $P(\rho) = \mathrm{Tr}(\rho^2)$ and fidelity to the target state $|\psi\rangle$, $F(\rho,\psi) = \langle\psi|\rho|\psi\rangle$. Note that there are several common definitions of fidelity in the literature, and our definition is the square of the fidelity used in refs 18 and 24. The quoted values significantly extend the state of the art for solid-state entanglement[18], and provide evidence that we have a high-fidelity universal set of two-qubit gates.

One- and two-qubit gates can be concatenated to realize simple algorithms, such as Grover's quantum search[1,2] shown in Fig. 4. Given a function $f(x)$ on the two-bit set $x \in \{00, 01, 10, 11\}$ such that $f(x) = 0$ except at some x_0, where $f(x_0) = 1$, this well-known algorithm can determine x_0 with a single call of an oracle O that encodes

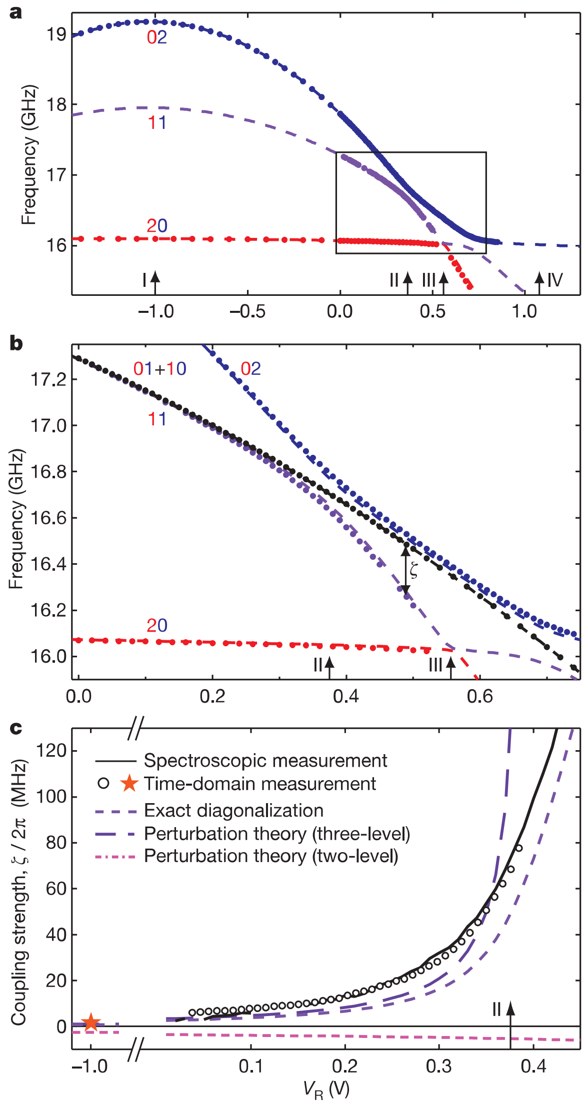

Figure 2 | Origin and characterization of the controlled-phase gate. a, Flux dependence of transition frequencies from the ground state $|0, 0\rangle$ to the two-excitation manifold. Red (blue) numerals indicate the excitation level of the left (right) transmon for each transition. Two-tone spectroscopy measurements[12] (points) show an avoided crossing between the computational state $|1, 1\rangle$ and the non-computational state $|0, 2\rangle$ at point II, in good agreement with numerical diagonalization of the Hamiltonian (dashed curves). **b,** This avoided crossing causes the transition frequency to $|1, 1\rangle$ to deviate from the sum of the transition frequencies to $|0, 1\rangle$ and $|1, 0\rangle$. **c,** The coupling strength $\zeta/2\pi = f_{01} + f_{10} - f_{11}$ of the effective $\sigma_z^L \otimes \sigma_z^R$ interaction, obtained both from spectroscopy (solid curve) and from time-domain experiments (points; see text for details). Numerical diagonalization and perturbation theory (Supplementary Information) for three-level transmons agree reasonably with data. The perturbation calculation diverges at the avoided crossing. Perturbation theory for two-level qubits gives the wrong magnitude and sign for ζ, and demonstrates that the higher transmon excitations are necessary for the interaction. Time-domain measurement and theory both give $\zeta/2\pi \approx 1.2$ MHz at point I. The tunability of ζ over two orders of magnitude provides an excellent on-off ratio for the two-qubit C-Phase gate.

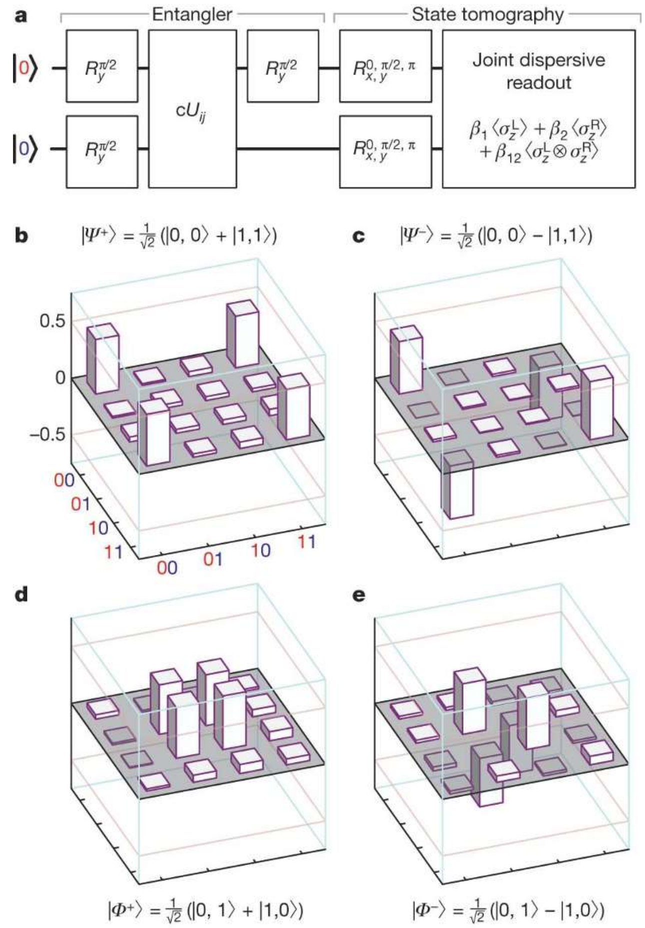

Figure 3 | Entanglement on demand. a, Gate sequence generating two-qubit entanglement and detection via quantum state tomography. Starting from $|0, 0\rangle$, simultaneous $\pi/2$ rotations on both qubits create an equal superposition of the four computational states. A C-Phase cU_{ij} then phase shifts $|i, j\rangle$ in the superposition and produces entanglement. A final $\pi/2$ rotation on Q_L evolves the entangled state into one of the four Bell states depending on the cU_{ij} applied. **b–e,** Real part of maximum-likelihood density matrix ρ_{ml} of the entangler output for cU_{10}, cU_{00}, cU_{11} and cU_{01}, respectively (imaginary elements of ρ_{ml} are less than 0.03, 0.02, 0.07, 0.08). Extracted metrics for the four entangler outputs include concurrence $C = 0.88 \pm 0.02$, 0.94 ± 0.01, 0.86 ± 0.02, 0.81 ± 0.04, purity $P = 0.87 \pm 0.02$, 0.92 ± 0.02, 0.88 ± 0.02, 0.79 ± 0.03, and fidelity to the ideal Bell state $F = 0.91 \pm 0.01$, 0.94 ± 0.01, 0.90 ± 0.01, 0.87 ± 0.02. The uncertainties correspond to the standard deviation in 16 repetitions of generation-tomography for each entangler.

$f(x)$ in a quantum phase, $O\,|x\rangle = (-1)^{f(x)}|x\rangle$. The oracle for $x_0 = ij$ is the C-Phase gate cU_{ij}.

We can examine the functioning of the algorithm by interrupting it after each step and performing state tomography. Figure 4b–g shows all the features of a quantum processor, namely the use of maximally superposed states to exploit quantum parallelism (Fig. 4c), the encoding of information in the entanglement between qubits (Fig. 4d, e), and the interference producing an answer represented in a final computational basis state. The fidelity of the final state (Fig. 4g) to the expected output ($|1, 0\rangle$ for the case $O = cU_{10}$ shown) is 85%. Similar performance is obtained for the other three oracles (Table 1).

We have also implemented the Deutsch–Jozsa algorithm[1,2]. The two-qubit version of this algorithm determines whether an unknown function $f_i(x)$, mapping a one-bit input to a one-bit output, is constant ($f_0(x) = 0$ or $f_1(x) = 1$) or balanced ($f_2(x) = x$ or $f_3(x) = 1 - x$) with a single call of the function. The algorithm applies the function once to a superposition of the two possible inputs and uses quantum phase kick-back[2] to encode the result in the final state of one qubit (Q_L) while leaving the other untouched (Q_R). The gate sequence realizing the algorithm and the output tomographs for the four cases are shown in Supplementary Fig. 1.

The performance of both algorithms is summarized in Table 1. Although there are undoubtedly significant systematic errors remaining, the overall fidelity is similar to that expected from the ratio (~100 ns/1 μs) of the total duration of gate sequences to the qubit coherence times. The detailed error budget will be addressed in future work using quantum process tomography.

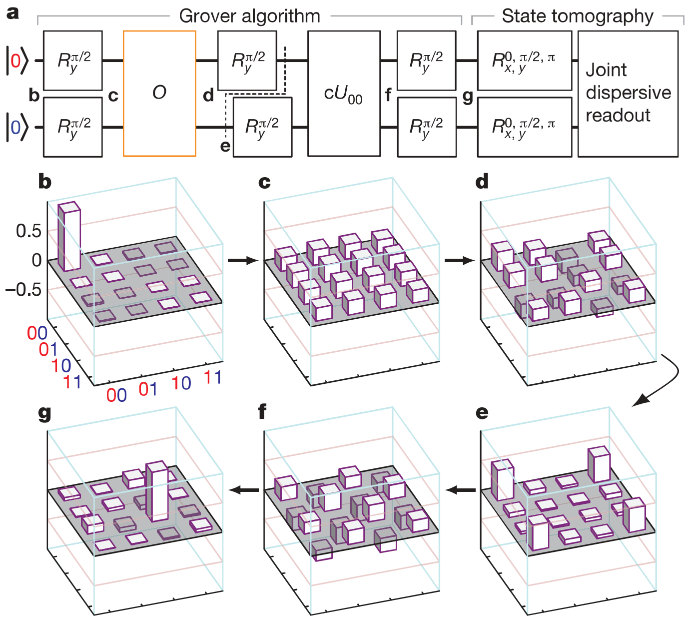

Figure 4 | Implementation of Grover's search algorithm. a, Concatenation of single-qubit and C-Phase gates implementing one iteration of Grover searching. Without loss of generality, we have replaced the Walsh–Hadamard transformations $W = R_x^{\pi} R_y^{\pi/2}$ in the usual description of the algorithm[1,2] with $R_y^{\pi/2}$ rotations in order to eliminate six single-qubit rotations and complete the sequence in 104 ns. (Supplementary Fig. 3 shows the microwave and flux pulses implementing the sequence.) The orange box is the oracle $O = \mathrm{c}U_{ij}$ that encodes the solution $x_0 = ij$ to the search problem in a quantum phase. Note that the first half of the algorithm is identical to the entangling sequence in Fig. 3, while the second half is essentially its mirror image. **b–g**, Real part of ρ_{ml} obtained by state tomography after each step of the algorithm with oracle $O = \mathrm{c}U_{10}$. Starting from $|0, 0\rangle$ (**b**), the qubits are simultaneously rotated into a maximal superposition state (**c**). The oracle then marks the solution, $|1, 0\rangle$, by inverting its phase (**d**). The $R_y^{\pi/2}$ rotation on Q_L turns the state into the Bell state $|\Psi^+\rangle$, demonstrating that the state is highly entangled at this stage. The $R_y^{\pi/2}$ rotation on Q_R produces a state identical to (**d**) (data not shown). The application of $\mathrm{c}U_{00}$ undoes the entanglement, producing a maximal superposition state (**f**). The final rotations yield an output state (**g**) with fidelity $F = 85\%$ to the correct answer, $|1, 0\rangle$.

In summary, we have demonstrated two-qubit quantum algorithms using a superconducting circuit. The incorporation of local flux control and joint-dispersive readout into cQED, together with a tenfold increase in qubit coherence over previous two-qubit devices, has enabled on-demand generation and detection of entanglement and the implementation of the Grover and Deutsch–Jozsa algorithms. The present architecture can be immediately expanded to several qubits with controllable $\sigma_z \otimes \sigma_z$ interactions between nearest-frequency neighbours, placing within reach the generation of Greenberger–Horne–Zeilinger states and the exploration of basic concepts of quantum error correction[1,2].

METHODS SUMMARY

Device fabrication. A 180 nm Nb film was d.c.-magnetron sputtered on the epi-polished surface of an R-plane corundum (α-Al_2O_3) wafer (2 inches diameter, 430 μm thickness). Coplanar waveguide structures (cavity and flux-bias lines) were patterned by optical lithography and fluorine-based reactive ion etching of Nb. Transmon features (interdigitated capacitors and split junctions) were patterned on 2 mm × 7 mm chips using electron-beam lithography, double-angle evaporation of Al (20/90 nm) with intermediate oxidation (15% O_2 in Ar at 15 torr for 12 min), and lift-off.

A completed device was cooled to 13 mK in a ^{3}He-^{4}He dilution refrigerator. The refrigerator wiring is shown in Supplementary Fig. 2. Careful microwave engineering of the sample holder and on-chip wirebonding across ground planes were required to suppress spurious resonance modes on- and off-chip. Simulations using Sonnet software assisted this iterative process. The sample was enclosed in two layers of Cryoperm magnetic shielding, allowing high-fidelity operation of the processor during unattended overnight runs.

cQED theory. The Tavis–Cummings[28] Hamiltonian generalized to multi-level transmon qubits[26] is:

$$H = \omega_{\mathrm{C}} a^{\dagger} a + \sum_{q \in \{\mathrm{L,\,R}\}} \left(\sum_{j=0}^{N} \omega_{0j}^{q} |j\rangle_q \langle j|_q + (a + a^{\dagger}) \sum_{j,k=0}^{N} g_{jk}^{q} |j\rangle_q \langle k|_q \right) \quad (1)$$

Here, ω_{C} is the bare cavity frequency, $\omega_{0j}^{q} = \omega_{0j}(E_{\mathrm{C}q}, E_{\mathrm{J}q})$ is the transition frequency for qubit q from ground to excited state j, and $g_{jk}^{q} = g_q n_{jk}(E_{\mathrm{C}q}, E_{\mathrm{J}q})$, with g_q a bare qubit–cavity coupling and n_{jk} a level-dependent coupling matrix element. The dependence of these parameters on qubit charging energy $E_{\mathrm{C}q}$ and Josephson energy $E_{\mathrm{J}q}$ is indicated. The flux control enters through $E_{\mathrm{J}q} = E_{\mathrm{J}q}^{\max} |\cos(\pi \Phi_q / \Phi_0)|$, with Φ_q the flux through the qubit loop, and a linear flux–voltage relation $\Phi_q = \alpha_{q\mathrm{L}} V_{\mathrm{L}} + \alpha_{q\mathrm{R}} V_{\mathrm{R}} + \Phi_{q,0}$, accounting for crosstalk and offsets. (Crosstalk, ~30%, probably results from spatial distribution of flux-bias return currents on the ground plane.) The above parameters are tightly constrained by the spectroscopy and transmission data shown (Figs 1b, 2a and b) and transmission data (not shown) for the Q_{L}-cavity vacuum Rabi splitting. Simultaneously fitting the spectra given by numerical diagonalization of the Hamiltonian (truncated to $N = 5$ qubit levels and 5 cavity photons) to these data gives $E_{\mathrm{JL(R)}}^{\max}/h = 28.48(42.34)$ GHz, $E_{\mathrm{CL(R)}}/h = 317(297)$ MHz, $g_{\mathrm{L(R)}}/2\pi = 199(183)$ MHz. Cavity parameters are $\omega_{\mathrm{C}}/2\pi = 6.902$ GHz and linewidth $\kappa/2\pi = 1$ MHz.

Received 11 March; accepted 5 May 2009.
Published online 28 June.

1. Nielsen, M. A. & Chuang, I. L. *Quantum Computation and Quantum Information* (Cambridge Univ. Press, 2000).
2. Kaye, P., Laflamme, R. & Mosca, M. *An Introduction to Quantum Computing* (Oxford Univ. Press, 2007).
3. Chuang, I. L., Vandersypen, L. M. K., Zhou, X., Leung, D. W. & Lloyd, S. Experimental realization of a quantum algorithm. *Nature* **393**, 143–146 (1998).
4. Jones, J. A., Mosca, M. & Hansen, R. H. Implementation of a quantum search algorithm on a quantum computer. *Nature* **393**, 344–346 (1998).
5. Chuang, I. L., Gershenfeld, N. & Kubinec, M. Experimental implementation of fast quantum searching. *Phys. Rev. Lett.* **80**, 3408–3411 (1998).
6. Guide, S. *et al.* Implementation of the Deutsch-Jozsa algorithm on an ion-trap quantum computer. *Nature* **421**, 48–50 (2003).
7. Brickman, K.-A. *et al.* Implementation of Grover's quantum search algorithm in a scalable system. *Phys. Rev. A* **72**, 050306(R) (2005).

Table 1 | Summary of algorithmic performance

Element		Grover search oracle*				Deutsch–Jozsa function†			
		f_{00}	f_{01}	f_{10}	f_{11}	f_0	f_1	f_2	f_3
⟨0,0|ρ|0,0⟩	Ideal	1	0	0	0	0	0	1	1
	Measured	0.81(1)	0.08(1)	0.07(2)	0.065(7)	0.010(3)	0.014(5)	0.909(6)	0.841(9)
⟨0,1|ρ|0,1⟩	Ideal	0	1	0	0	0	0	0	0
	Measured	0.066(7)	0.802(9)	0.05(1)	0.054(8)	0.012(4)	0.008(4)	0.031(8)	0.04(2)
⟨1,0|ρ|1,0⟩	Ideal	0	0	1	0	1	1	0	0
	Measured	0.08(1)	0.05(1)	0.82(2)	0.07(1)	0.93(1)	0.93(1)	0.05(1)	0.04(1)
⟨1,1|ρ|1,1⟩	Ideal	0	0	0	1	0	0	0	0
	Measured	0.05(2)	0.07(1)	0.06(1)	0.81(1)	0.05(1)	0.04(1)	0.012(9)	0.07(2)

Fidelity of the reconstructed output states of the Grover and Deutsch–Jozsa algorithms to their ideal outputs. These results suggest that, if combined with single-shot readout, the two algorithms executed with this processor would give the correct answer with probability far exceeding the 50% success probability of the best classical algorithms limited to single calls of the oracle[7] or function.
* Uncertainties are based on 10 repetitions.
† Uncertainties are based on 8 repetitions.

8. Kwiat, P. G., Mitchell, J. R., Schwindt, P. D. D. & White, A. G. Grover's search algorithm: an optical approach. *J. Mod. Opt.* **47**, 257–266 (2000).
9. Blais, A., Huang, R.-S., Wallraff, A., Girvin, S. M. & Schoelkopf, R. J. Cavity quantum electrodynamics for superconducting electrical circuits: an architecture for quantum computation. *Phys. Rev. A* **69**, 062320 (2004).
10. Wallraff, A. *et al.* Strong coupling of a single photon to a superconducting qubit using circuit quantum electrodynamics. *Nature* **431**, 162–167 (2004).
11. Clarke, J. & Wilhelm, F. K. Superconducting quantum bits. *Nature* **453**, 1031–1042 (2008).
12. Schreier, J. A. *et al.* Suppressing charge noise decoherence in superconducting charge qubits. *Phys. Rev. B* **77**, 180502(R) (2008).
13. Lucero, E. *et al.* High-fidelity gates in a single Josephson qubit. *Phys. Rev. Lett.* **100**, 247001 (2008).
14. Chow, J. M. *et al.* Randomized benchmarking and process tomography for gate errors in a solid-state qubit. *Phys. Rev. Lett.* **102**, 090502 (2009).
15. Yamamoto, T., Pashkin, Yu. A., Astafiev, O., Nakamura, Y. & Tsai, J. S. Demonstration of conditional gate operation using superconducting charge qubits. *Nature* **425**, 941–944 (2003).
16. Plantenberg, J. H., de Groot, P. C., Harmans, C. J. P. M. & Mooij, J. E. Demonstration of controlled-NOT quantum gates on a pair of superconducting quantum bits. *Nature* **447**, 836–839 (2007).
17. Niskanen, A. O. *et al.* Quantum coherent tunable coupling of superconducting qubits. *Science* **316**, 723–726 (2007).
18. Steffen, M. *et al.* Measurement of the entanglement of two superconducting qubits via state tomography. *Science* **313**, 1423–1425 (2006).
19. Siddiqi, I. *et al.* RF-driven Josephson bifurcation amplifier for quantum measurement. *Phys. Rev. Lett.* **93**, 207002 (2004).
20. McDermott, R. *et al.* Simultaneous state measurement of coupled Josephson phase qubits. *Science* **307**, 1299–1302 (2005).
21. Sillanpää, M. A., Park, J. I. & Simmonds, R. W. Coherent quantum state storage and transfer between two phase qubits via a resonant cavity. *Nature* **449**, 438–442 (2007).
22. Majer, J. *et al.* Coupling superconducting qubits via a cavity bus. *Nature* **449**, 443–447 (2007).
23. Schuster, D. I. *et al.* Resolving photon number states in a superconducting circuit. *Nature* **445**, 515–518 (2007).
24. Filipp, S. *et al.* Two-qubit state tomography using a joint dispersive read-out. *Phys. Rev. Lett.* **102**, 200402 (2009).
25. Houck, A. A. *et al.* Controlling the spontaneous emission of a superconducting transmon qubit. *Phys. Rev. Lett.* **101**, 080502 (2008).
26. Koch, J. *et al.* Charge-insensitive qubit design derived from the Cooper pair box. *Phys. Rev. A* **76**, 042319 (2007).
27. Blais, A. *et al.* Quantum-information processing with circuit quantum electrodynamics. *Phys. Rev. A* **75**, 032329 (2007).
28. Tavis, M. & Cummings, F. W. Exact solution for an *N*-molecule-radiation-field Hamiltonian. *Phys. Rev.* **170**, 379–384 (1968).
29. Strauch, F. W. *et al.* Quantum logic gates for coupled superconducting phase qubits. *Phys. Rev. Lett.* **91**, 167005 (2003).
30. Wootters, W. K. Entanglement of formation of an arbitrary state of two qubits. *Phys. Rev. Lett.* **80**, 2245–2248 (1998).

Supplementary Information is linked to the online version of the paper at www.nature.com/nature.

Acknowledgements We thank V. Manucharyan and E. Boaknin for experimental contributions, and M. H. Devoret, I. L. Chuang and A. Nunnenkamp for discussions. This work was supported by LPS/NSA under ARO contract W911NF-05-1-0365, and by the NSF under grants DMR-0653377 and DMR-0603369. We acknowledge additional support from CIFAR, MRI, MITACS and NSERC (J.M.G.), NSERC, CIFAR and the Alfred P. Sloan Foundation (A.B.), and from CNR-Istituto di Cibernetica, Pozzuoli, Italy (L.F.).

Author Information Reprints and permissions information is available at www.nature.com/reprints. Correspondence and requests for materials should be addressed to R.J.S. (robert.schoelkopf@yale.edu).